Journal of Geophysical Research: Space Physics

RESEARCH ARTICLE
10.1029/2018JA025720

# Oscillation of the Ionosphere at Planetary-Wave Periods

**J. M. Forbes[1], A. Maute[2], X. Zhang[1], and M. E. Hagan[3]**

[1]Ann and H.J. Smead Department of Aerospace Engineering Sciences, University of Colorado Boulder, Boulder, CO, USA, [2]High Altitude Observatory, National Center for Atmospheric Research, Boulder, CO, USA, [3]Department of Physics, Utah State University, Logan, UT, USA

**Key Points:**
- Ionospheric oscillations occur at planetary-wave (PW) periods (2–20 days) due to PW modulation of the upward-propagating tidal spectrum
- A new mechanism for PW coupling in the atmosphere-ionosphere system is discovered
- Zonally symmetric oscillations account for roughly half the ionospheric perturbations at PW periods

**Supporting Information:**
- Supporting Information S1

**Correspondence to:**
J. M. Forbes,
forbes@colorado.edu

**Citation:**
Forbes, J. M., Maute, A., Zhang, X., & Hagan, M. E. (2018). Oscillation of the ionosphere at planetary-wave periods. *Journal of Geophysical Research: Space Physics*, *123*. https://doi.org/10.1029/2018JA025720

Received 25 MAY 2018
Accepted 25 JUL 2018
Accepted article online 6 AUG 2018

**Abstract** F-region ionospheric oscillations at planetary-wave (PW) periods (2–20 days) are investigated, with primary focus on those oscillations transmitted to the ionosphere by PW modulation of the vertically propagating tidal spectrum. Tidal effects are isolated by specifically designed numerical experiments performed with the National Center for Atmospheric Research thermosphere-ionosphere-electrodynamics general circulation model for October 2009, when familiar PW and tides are present in the model. Longitude versus day-of-month perturbations in topside F-region electron density (Ne) of order ±30–50% at PW periods occur as a result of PW-modulated tides. At a given height, these oscillations are mainly due to vertical oscillations in the F layer of order ±15–40 km. These vertical movements are diagnosed in terms of changes in the F2-layer peak height, ΔhmF2, which are driven by the vertical projections of E × B drifts and field-aligned in situ neutral winds. E × B drifts dominate at the magnetic equator, while the two sources play more equal roles between 20° and 40° magnetic latitudes in each hemisphere. The in situ neutral wind effect arises from vertical propagation of PW-modulated tides, whereas the E × B drifts originate from dynamo-generated electric fields produced by the E-region component of the same wind field; the former represents a new coupling mechanism for production of ionospheric oscillations at PW periods. Roughly half the above-mentioned variability in Ne and hmF2 is associated with zonally symmetric (S0) oscillations, which contribute at about half the level of low-level magnetic activity during October 2009. The thermosphere-ionosphere-electrodynamics general circulation model simulates the S0 oscillations in Ne observed from the CHAMP satellite well during this period and reveals that S0 oscillations in E × B play a significant role in driving S0 oscillations in ΔhmF2, in addition to neutral winds.

## 1. Introduction

Oscillation of the F-region ionosphere at planetary-wave (PW) periods (2–20 days), originating from stratosphere and mesosphere PW, has been the subject of research for at least three decades. Most attention has been devoted to the *normal mode* (NM) or *quasi-resonant* westward-propagating PW oscillations with periods (zonal wavenumbers) near 2 ($s = 3$), 6 ($s = 1$), 10 ($s = 1$), and 16 days ($s = 1$; Salby, 1981; see also Forbes, 1995). In the more recent literature, these are referred to as the quasi-2-day wave (Q2DW), Q6DW, Q10DW, and Q16DW, recognizing that at any given time, the precise period may differ from precisely 2, 6, 10, or 16 days.

Ito et al. (1986) were the first to suggest that the Q2DW could modulate the ionospheric wind dynamo. Motivated by prior mesospheric observations of quasi-2-day variations in mesospheric winds and in ground magnetic perturbations, they produced dynamo simulations of a Q2DW-modulated Sq current system consistent with these other observations. Shortly thereafter, Chen (1992; with references to his 1987, 1989, 1990, and 1991 publications in the Chinese literature) presented observational evidence and numerical simulations of Q2DW variations in the equatorial ionization anomaly. This work was motivated by the observed day-to-day variability of the equatorial ionization anomaly as documented in Huang et al. (1989). Contemporaneous research on Q2DW oscillations in the midlatitude ionosphere was also being conducted within this time frame (Pancheva, 1988; Pancheva & Lysenko, 1988).

During the 1990s, additional papers subsequently appeared that documented PW variations in the ionosphere (e.g., Altadill et al., 1997; Altadill & Lastovicka, 1996; Apostolov et al., 1994, 1995; Forbes et al., 1997; Forbes & Leveroni, 1992; Forbes & Zhang, 1997; Laštovička & Šauli, 1999; Pancheva et al., 1994; Parish et al., 1994). However, numerical simulations of the Q2DW (Hagan et al., 1993) and Q16DW (Forbes et al., 1995) suggested that PW did not penetrate into the dynamo region, prompting a review of potential mechanisms

©2018. American Geophysical Union. All Rights Reserved.

for imposing PW periodicities on the ionosphere (Forbes, 1996). Besides direct penetration into the dynamo region (Pancheva & Lysenko, 1988), these mechanisms included PW-induced changes in composition, that is, $[O]/[N_2]$ and $[O]/[O_2]$ ratios (Pancheva & Lysenko, 1988); PW modulation of tides, which then impose variability at PW periods in the dynamo region (Chen, 1992); and secondary generation of PW in the dynamo region due to dissipation of gravity waves (GW) that are modulated by PW winds at lower altitudes (Forbes, 1996), by analogy with a similar interaction between GW and stationary PW (McLandress & Mcfarlane, 1993; Miyahara, 1985). During this period Meyer (1999) presented numerical simulations to show that secondary excitation of PW due to dissipation of PW-modulated GW between 100 and 150 km was a viable mechanism to facilitate penetration of Q2DW and Q16DW oscillations into the dynamo region.

During the following decade (2000–2010), observational studies of PW-period oscillations in the ionosphere continued (e.g., Altadill, 2000; Altadill et al., 2001, 2003; Borries & Hoffmann, 2010; Borries et al., 2007; Laštovička et al., 2006), often citing contemporaneous observations of similar-period oscillations in the stratosphere and/or mesosphere. However, it was also recognized that ionospheric variations at PW periods associated with magnetic or solar activity were an issue that had to be dealt with. In particular, recurrent magnetic activity associated with high-speed streams emanating from coronal holes on the Sun (Lei et al., 2008) occurs at subharmonics of the 27-day solar rotation (i.e., 13.5, 9, 6.75, and 5.4 days), overlapping with periods of the atmospheric NM mentioned previously. The Borries and Hoffmann (2010) study is particularly noteworthy due to the care with which they removed solar and geomagnetic effects and the fact that the authors analyzed an array of data covering the hemisphere poleward of 50°N. The latter enabled them to separate zonally symmetric, eastward-, and westward-propagating oscillations. Interestingly, they found the dominant oscillations to be zonally symmetric with periods between about 2 and 16 days. This decade also included efforts to more generally quantify ionospheric variability due to *meteorological influences* both observationally (Forbes et al., 2000; Rishbeth & Mendillo, 2001) and through theory and modeling (Mendillo et al., 2002; Rishbeth, 2006; Rishbeth et al., 2009; see also Liu et al., 2013).

In summary, research prior to about 2010 provided evidence for PW-driven oscillations of the ionosphere and their connections to troposphere and/or middle atmosphere dynamics. This work was foundational for research in the current decade, which has focused on illumination of the physical processes involved in PW-ionosphere coupling. This has largely been made possible by the development and application of first-principles general circulation models that solve the coupled equations governing the energetics, dynamics, electrodynamics, and chemistry of the stratosphere, mesosphere, thermosphere, and ionosphere. For instance, authors used the National Center for Atmospheric Research thermosphere-ionosphere-mesosphere-electrodynamics general circulation model (TIME-GCM) to demonstrate that PW themselves can penetrate above 100 km to produce dynamo electric fields that drive Q2DW (Yue et al., 2012, 2016) and Q6DW (Gan et al., 2016, 2017) F-region ionospheric variability, although it is recognized that such penetration is highly sensitive to the zonal-mean wind distribution above 100 km, which is poorly known. In addition, Yue et al. (2016), Gan et al. (2017), and Gu et al. (2018) show that the nonlinear interaction between PW and tides and the secondary waves that arise from these interactions play an important role in how the ionosphere responds. Other studies have shown that the dissipation of PW (Chang et al., 2014; Gan et al., 2015; Yue & Wang, 2014) or changes in turbulent mixing arising from PW modulation of GW (Nguyen & Palo, 2014) can induce chemical changes that translate to ionospheric variations, either at PW periods or in the net response.

Although the above studies have demonstrated that PW can drive significant F-region effects due to composition changes and dynamo-generated electric fields, the individual effects of PW versus tides have not been unequivocally separated; that is, whether the PW itself penetrates sufficiently into the dynamo region to produce effective E fields or whether the PW periodicity is imposed on the ionosphere by atmospheric tides that are modulated by PW. In the latter case, we must then consider the possibility that in situ winds in the F region due to vertically penetrating tides might also modulate the ionosphere at PW periods. In addition, most studies so far have considered single PW (i.e., Q2DW or Q6DW) and a tidal spectrum that is fixed in time, that is, in the context of diurnally reproducible (steady-state) simulations. As described in more detail below, the present paper addresses all of the above aspects of the problem.

In a prelude to the current paper, the present authors (Forbes et al., 2018; hereafter paper I) used the output of a TIME-GCM simulation forced at its 30-km lower boundary by a 3-hourly global reanalysis product (Häusler et al., 2014, 2015; see also Nystrom et al., 2018), to serve as the 97-km lower boundary condition

for thermosphere-ionosphere-electrodynamics general circulation model (TIE-GCM) numerical experiments that isolated the ionosphere-thermosphere response to different parts of the PW-tide spectrum. The focus was on the October 2009 period which was characterized by presence of the Q6DW, Q10DW, Q16DW, and an ultrafast Kelvin wave (UFKW) with period near 3.5 days and $s = -1$. By differencing different TIE-GCM outputs, the effects of tides on the thermosphere response were able to be isolated. Since the tidal spectrum was modulated by a spectrum of PW, the degree to which wind, temperature, and density variations in the thermosphere at PW periods could result from PW-modulated tides alone could be established.

Several new results emerged from paper I, which focused on the neutral atmosphere response. First, much of the response consisted of zonally symmetric ($s = 0$, hereafter S0) oscillations at PW periods between 3 and 20 days. This was explained in terms of vacillation of the zonal-mean state (temperature, winds, density, and composition) resulting from heat flux and momentum flux divergences due to dissipation of the PW-modulation tidal spectrum. However, there were also sizable ($\pm 40$ ms$^{-1}$) universal time (UT)-longitude variations in neutral winds at 120 km at PW period and with $s \neq 0$ produced by the tides that have obvious ionospheric implications, at least in terms of potential dynamo electric field generation. In addition, there were significant wind and composition variations at F-region heights that remained to be explored in terms of ionospheric consequences. The purpose of this paper is to investigate and report on the ionospheric consequences of the simulations discussed in paper I. In light of the paper I results and the discovery of significant S0 oscillations of the ionosphere at PW periods by Borries and Hoffmann (2010), some attention is devoted to S0 ionospheric oscillations. Also, the paper I simulations were performed during a period of low but variable magnetic activity, which provides the opportunity to examine and separate this source of PW-period variability from that of meteorological origin, replicating the situation typically encountered in observational studies of the phenomenon. For later reference, supporting information Figures S0a and S0b provide plots and wavelet spectra of Kp, Ap, and F10.7 for October 2009 that replicate and augment those provided in paper I.

The following section describes the paper I numerical experiments in more detail. Section 3.1 presents our results in terms of electron density (Ne) variability at 325 km (the mean altitude of CHAMP during October 2009), while section 3.2 explains this variability in terms of PW-period variations in neutral winds, plasma drifts, and composition variations. PW-period variations in Ne measured by CHAMP are compared with TIE-GCM output, which is then used to separate effects due to PW-tide modulation and geomagnetic activity. Concluding remarks are provided in section 4.

## 2. Numerical Experiments

Since the model suite used to perform the simulations and numerical experiments in the present paper are described fully in paper I (see also Nystrom et al., 2018), including citations to the relevant literature, the following is an abbreviated description. The models involved are the National Center for Atmospheric Research TIME-GCM, the TIE-GCM, and the Modern-Era Retrospective Analysis for Research and Applications (MERRA). TIME-GCM solves the equations governing the energetics, dynamics, chemical composition, and electrodynamics of the neutral and ionized components of the atmosphere from a constant pressure level near 30 km to about 500–800 km depending on level of solar activity. As described in Häusler et al. (2014, 2015), a specific TIME-GCM simulation was created (hereafter TIME-GCM/MERRA2009) wherein the lower boundary forcing at 30 km consisted of 3-hourly output from MERRA for all of 2009. Since MERRA is a physics-based weather prediction model constrained by global assimilated data, it provides realistic forcings of meteorological origins to the TIME-GCM at time scales of 8 hr and greater; it thus includes diurnal and semidiurnal tides, Kelvin waves, planetary Rossby waves, and stationary planetary waves. In the current work we use TIME-GCM/MERRA2009 output to impose this variability on the TIE-GCM, a model similar to the TIME-GCM except that its lower boundary is at a constant pressure level 97 km. The reason for coupling these two models together in this fashion is described below.

Our interest in the present paper is to quantify the degree to which variability at PW periods is transmitted to the ionosphere by the lower atmosphere and to better understand the processes through which this coupling occurs. To do this, we filtered the TIME-GCM/MERRA2009 output to isolate different parts of the wave spectrum and used these wave outputs to drive the TIE-GCM in a way that enables us to isolate their individual effects by *differencing* the various TIE-GCM outputs. For instance, one numerical experiment consisted of forcing the TIE-GCM with daily diurnal and zonal means of TIME-GCM/MERRA2009 at each latitude; these include the S0 oscillations defined previously. Another simulation consisted of forcing the TIE-GCM

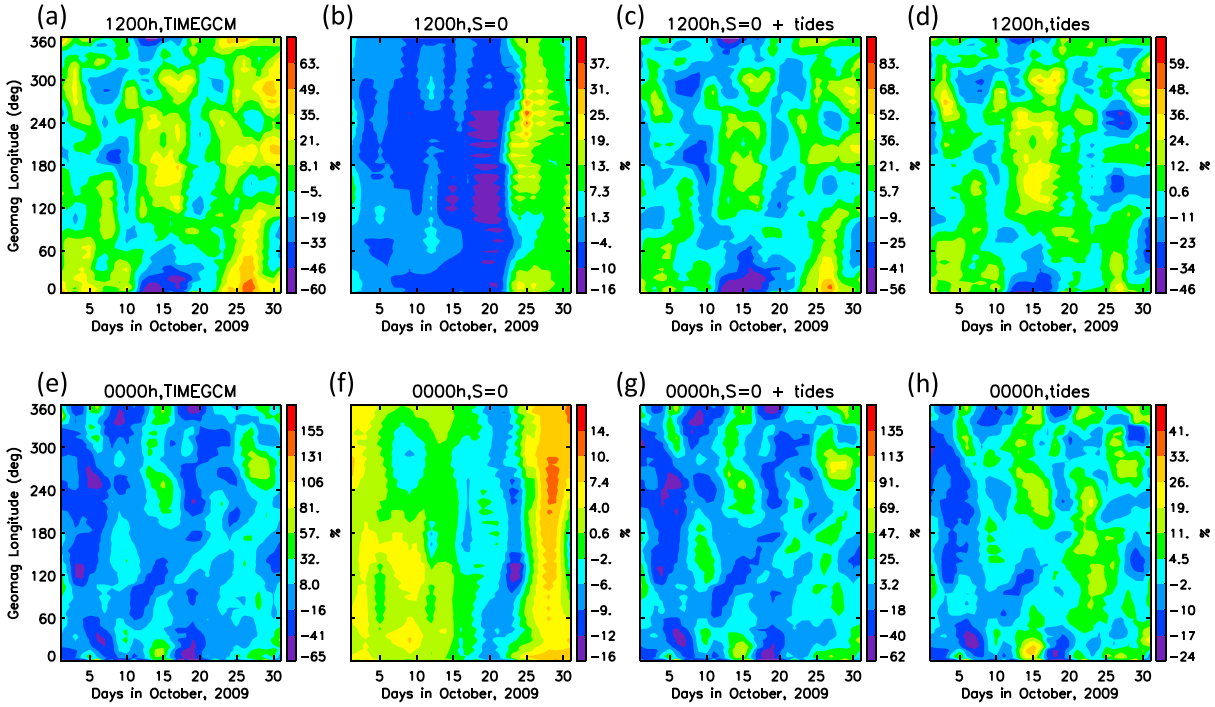


**Figure 1.** Examples of ΔNe responses as a function of longitude and day of month at 325 km due to different lower boundary forcing of the thermosphere ionosphere electrodynamics general circulation model, in this case at geomagnetic latitude −20° and local time = 1200 hr (top) and local time = 0000 hr (bottom). (a) and (e) Full TIME-GCM forcing at the lower boundary, that is, the reference simulation. (b) and (f) S0 forcing only. (c) and (g) S0 forcing plus tides. (d) and (h) Tide contribution alone. Similar figures at −40°, −20°, 0°, +20°, and +40° latitude are contained in Figure S1a.
TIME-GCM = thermosphere-ionosphere-mesosphere-electrodynamics general circulation model.

with daily S0 *plus* waves with periods between 2 and 7 days and zonal wavenumbers $s = +1$ and $s = -1$; the former includes the Q6DW, and the latter includes UFKW (Nystrom et al., 2018). By differencing the outputs of these two TIE-GCM simulations, the ionospheric responses to Q6DW and UFKW forcings are separated from those of S0 forcing. Other simulations that were performed included forcing by daily S0 + tides; daily S0 + tides + 2–7-day waves; and a *reference simulation* wherein the complete TIME-GCM/MERRA output at 97 km is used as input to the TIE-GCM. All of the above TIE-GCM simulations include solar and geomagnetic forcing within the thermosphere as parameterized by F10.7 and Kp variations.

The reader is referred to paper I and Nystrom et al. (2018) for extensive comparisons between TIME-GCM/MERRA2009 and ground-based and space-based measurements. These comparisons are accompanied by interpretations and justifications regarding the suitability of these models to provide a realistic framework for investigating the impacts of PW-tide interactions on the ionosphere-thermosphere system.

## 3. Results

### 3.1. Response Characteristics

All neutral atmosphere simulations to be discussed in the following were performed in geographic coordinates, and an internal mapping to the quasi-dipole magnetic coordinate system (Richmond, 1995; see also Laundal & Richmond, 2016) was performed to solve the electrodynamic equations. Results presented in Figures 1–5 are in the quasi-dipole coordinate system and designated *geomagnetic latitude* and geomagnetic longitude, as this is a more natural way to present and interpret E × B versus neutral wind contributions to changes in Ne and hmF2. As for paper I, the present study is confined to October 2009, for the reasons described in the previous section. In addition, all analyses and plots were performed for local times (LTs) of LT = 1200 hr, LT = 0000 hr, LT = 1600 hr, and LT = 0400 hr; the former to conform with paper I, and the latter to conform with comparisons with CHAMP data during October 2009. Similarly, results are presented for a fixed altitude of 325 km for consistency with paper I, and since this is close to the mean altitude of CHAMP during October 2009, this also provides the opportunity to highlight differences in how the response of the PW-modulated ionosphere is revealed in measurements at a fixed altitude or in total electron content. To

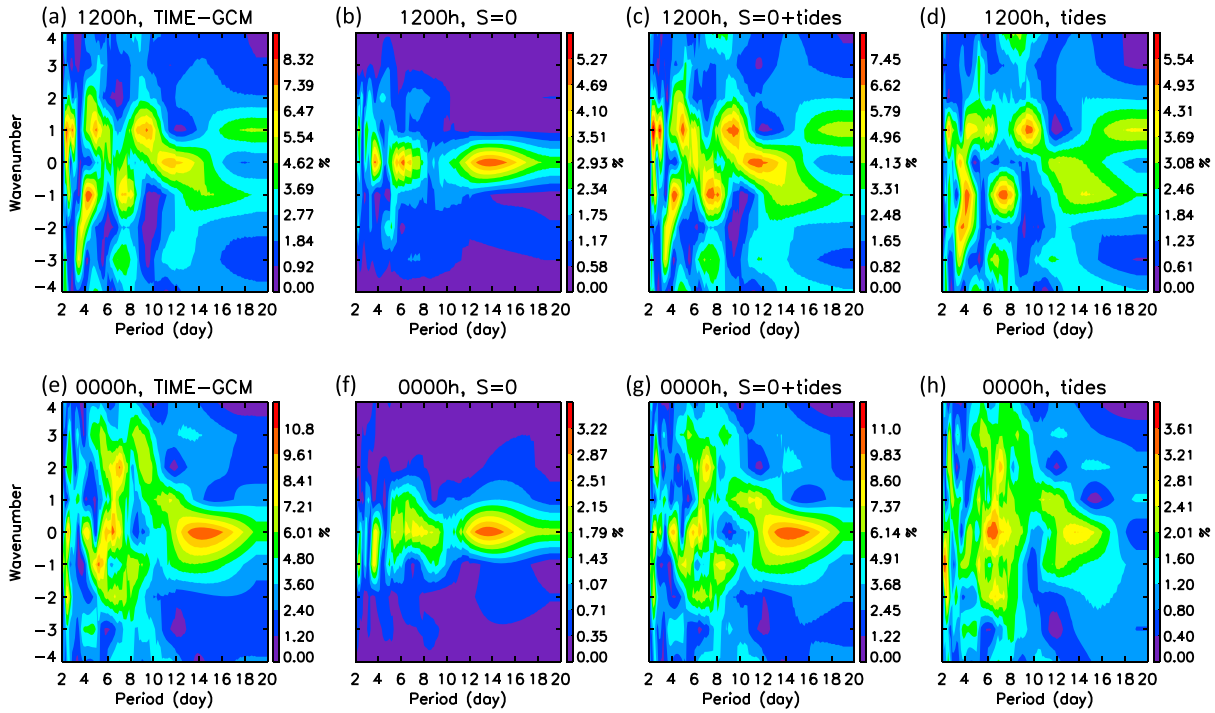


**Figure 2.** Same as Figure 1, except showing the wavenumber versus period spectrum for each panel. Similar figures at −40°, −20°, 0°, +2°, and +40° latitude are contained in Figure S2. TIME-GCM = thermosphere-ionosphere-mesosphere-electrodynamics general circulation model.

better highlight the day-to-day variability, quantities such as electron density (Ne) are expressed in terms of residuals from the 27-day running mean at a particular LT and designated with the prefix Δ, that is, ΔNe.

Figure 1 provides examples of the numerical experiments, in this case for magnetic latitude −20°. Each panel represents a depiction of ΔNe at 325 km, plotted as a function of magnetic longitude and day of month during October 2009. The top row (Figures 1a–1d) corresponds to LT = 1200 hr and the bottom row (Figures 1e–1h) to LT = 0000 hr. The left column (Figures 1a and 1e) depicts the TIE-GCM output with lower boundary forcing at 97 km defined according to the full TIME-GCM output (i.e., reference simulation). The second column (Figures 1b and 1f) represents the TIE-GCM simulation including S0 forcing only, both at the lower boundary and in situ within the thermosphere. The latter is the dominant S0 response, and in fact, the large negative and positive excursions in ΔNe around days 20–27 are associated with the increase in magnetic activity around this time (see Figures S0a and S0b and also Figure 6 in this paper and related discussion). Note that the ΔNe excursions resulting from S0 forcing alone are much smaller than those in the reference simulation, indicating that there is a source of PW-period variability that is missing in the S0-forced simulations. A small but non-negligible amount of this difference is taken up by the fact that the 27-day means due to S0 forcing only are somewhat larger than those for the reference simulations (see Figure S1b).

Figures1c and 1g depict the ΔNe variations resulting from the addition of tides to the lower boundary of the TIE-GCM and also include the S0 forcing mentioned above. Comparing Figures 1a and 1e with 1c and 1g, respectively, there is now a close match between amplitudes and phases of the ΔNe variability at PW period that results from inclusion of tides at the lower boundary of the TIE-GCM and that from the reference simulation. By taking grid point by grid-point differences between the S0 and S0 + tides simulations, the ΔNe residuals in Figures 1d and 1h, which are referenced to the 27-day running means of the S0 simulation, are obtained. These are the PW-period oscillations in ΔNe that result solely from the vertically propagation tides (modulated by PW) and amount to about ±40% at LT = 1200 hr and ±25% at LT = 0000 hr. The reader is reminded that the reference TIE-GCM simulation also includes PW forcing at its lower boundary. Therefore, the close match between Figures 1c and 1g and 1a and 1e also implies that the effects of PW alone on ΔNe are much smaller than those of the PW-modulated tides.

Figure S1a contains the same information as in Figure 1, except at −40°, −20°, 0° , +20°, and +40° latitudes. Figure S1b includes the corresponding figures for the 27-day running means of Ne, which form the basis for calculating the ΔNe residuals.

We now seek to better characterize and understand the origins of the ΔNe fluctuations depicted in Figure 1. Figure 2 depicts wavenumber versus period spectra of the ΔNe residuals in Figure 1. As expected, the spectra that correspond to numerical experiments that include S0 forcing only (Figures 1b and 1f) consist largely of an S0 response with periodicities that mainly reflect the spectral peaks in the wavelet depiction of Ap provided in Figure S0b. Referring back to the discussion in section 1 regarding coincidence of recurrent magnetic activity variability near the periods of atmospheric NM, we take difference fields to isolate the effects of PW-modulated tides from those due to magnetic activity. In addition to the predominant S0 responses, Figures 2b and 2f also contain signatures of weaker responses at similar periods that occur at $s = \pm 1$ and $\pm 2$ wavenumbers. Although Figures 1 and 2 are in magnetic coordinates, if the neutral dynamics driving the ΔNe variability is ordered in geographic coordinates, then the displacement between coordinate systems will introduce longitude variability in the form of *wavenumber broadening* as discussed by Yue et al. (2013). Similar considerations apply for the other spectra in Figure 2.

Another noteworthy point concerning Figure 2 is the similarity between spectra in the first column (Figures 2a and 2e) and third column (Figures 2c and 2g), which underscores the importance of tides in explaining both the longitude and PW-period variability of ΔNe. Also, especially for the LT = 0000-hr simulations, significant PW-period S0 responses occur as a result of tidal forcing alone. In principle, S0 oscillations in ΔNe can also result from wavenumber broadening, but as shown in paper I, the neutral thermosphere response to tidal forcing is manifested strongly in S0 oscillations which can be transmitted to the ionosphere through several mechanisms.

Figure S2 contains the same information as in Figure 2, except at −40°, −20°, 0° , +20°, and +40° latitudes.

### 3.2. Response Attributions

We now turn to the mechanisms through which tidal variability drives the ionospheric variability seen in the last columns of Figures 1 and 2. In a nonlinear self-consistent first-principles model such as the TIE-GCM, there are many interactive factors that come into play, such as neutral dynamics, electrodynamics, plasma-neutral interactions, neutral and ion chemistry, diffusion, temperature-dependent chemical reactions, and rates of diffusion, viscosity, and thermal conductivity. Our main goals here are to establish a dynamical connection between PW-modulated tides and PW-period variations in ΔNe that are produced in the F region by (a) E × B drifts and (b) neutral winds and to establish the degree to which any chemical effects are at play. Our reasoning is that the influence of E × B drifts versus neutral winds provides a measure of the relative importance of the dynamo-region wind field versus vertical penetration of PW-modulated tidal winds and thus provides new insights into the nature of the atmosphere-ionosphere coupling process. The broad nature of our objectives also permits a relatively simple approach.

At a fixed height of 325 km, changes in Ne are governed by the continuity equation:

$$\frac{\partial N_e}{\partial t} = P - L - \nabla \cdot N_e \vec{V}_e, \tag{1}$$

where $P$ and $L$ represent chemical production and loss, respectively, and $\vec{V}_e$ is the drift velocity of the electrons. In the low and middle latitude F region, it is commonplace to neglect horizontal transport and gradients as well as divergence of $\vec{V}_e$; as a good approximation, we have

$$\frac{\partial N_e}{\partial t} \approx P - L - w_e \frac{\partial N_e}{\partial z}, \tag{2}$$

changes in Ne are governed by the continuity where $w_e$ is the vertical velocity of the electrons (positive upward) and $z$ is altitude. Here $w_e$ can arise due to neutral winds along magnetic field lines, E × B drifts normal to B, or departures from equilibrium plasma diffusion. Above the F-region peak, the time constants for chemically induced changes in Ne are long compared with dynamics, leaving

$$\frac{\partial N_e}{\partial t} \approx -w_e \frac{\partial N_e}{\partial z}. \tag{3}$$

Above the F-region peak, $\frac{\partial Ne}{\partial z} < 0$ so that an upward (downward) motion of electrons, $w_e > 0 (w_e < 0)$, leads to an increase (decrease) in Ne; similarly, below the peak, $w_e > 0 (w_e < 0)$ leads to a decrease (increase) in Ne.

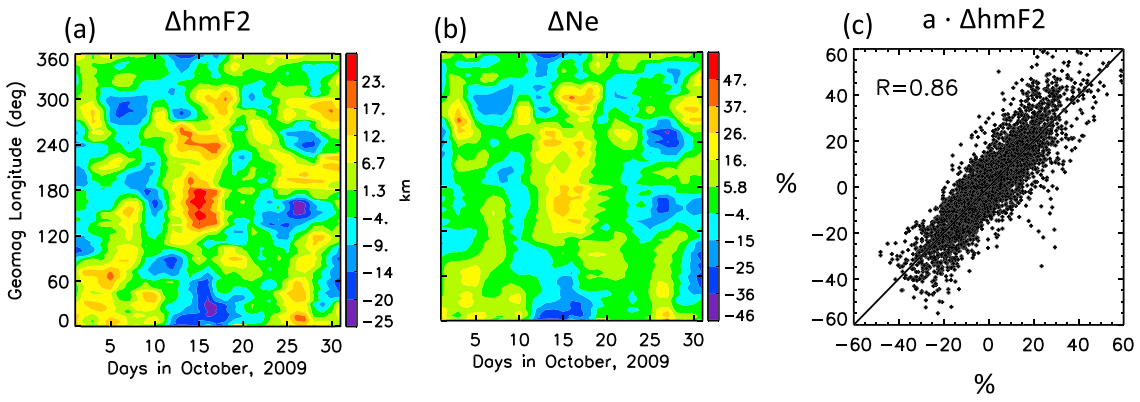


**Figure 3.** Example correlation between ΔNe and ΔhmF2, in this case for −20° geomagnetic latitude for local time = 1200 hr. (a) hmF2; (b) Ne; (c) scatter plot showing correlation between ΔNe and ΔhmF2. Similar figures at −40°, −20°, 0°, +20°, and +40° latitude are contained in Figure S3a.

Another way of thinking of this is in terms of the so-called servo model (Rishbeth, 1967, 1968; see also Buonsanto et al., 1997; Miller et al., 1986; Rishbeth et al., 1978) where $w_e$ moves the equilibrium height (hmF2) of the F-layer peak up or down depending on whether $w_e > 0$ or $w_e < 0$, respectively. At fixed heights sufficiently above or below hmF2, the two approaches yield similar results assuming the shape of the layer does not differ appreciably. The servo model is a conceptual framework well-suited for the current application since it has been widely used and tested; is applicable at low as well as middle latitudes (Gurubaran & Sridharan, 1993); yields a linear relationship between vertical drifts and hmF2 for the ranges of winds, drifts, and changes in hmF2 pertinent to the present study (Buonsanto et al., 1997; Gurubaran & Sridharan, 1993; Miller et al., 1986; Rishbeth et al., 1978); and is sufficient to achieve the above-stated goals. The magnetic equator is a special case, which is discussed further below.

In the present simulations, the only LTs where the servo-type model can be used to fully connect hmF2 variations with ΔNe variations is around noon, when hmF2 is sufficiently below 325 km. An example is provided in Figure 3 and corresponds to the *tides only* difference fields. (Figure S3a provides similar results, except at −40°, −20°, 0°, +20°, and +40° latitude.) Figure 3b replicates ΔNe from Figure 1d, while Figure 3a shows the hmF2 residuals (hereafter Δ*hmF*2) from 27-day means, processed exactly as the Ne variations in Figure 3b. The ±45% fluctuations in Ne correlate very well with the ±25-km excursions in Δ*hmF*2; this is obvious visually and is quantified in the scatter plot of Figure 3c which indicates a correlation coefficient $R = +0.86$. Note that the 27-day mean values of hmF2 (see Figure S3b) range between 235 ± 25 km over the same longitudes and days depicted in Figure 3. The corresponding correlation coefficients are $R = +0.84, +0.86, +0.66, +0.80$, and +0.83 at magnetic latitudes −40°, −20°, 0°, +20°, and +40°, respectively, and the corresponding ranges of hmF2 are 225 ± 20, 235 ± 25, 275 ± 30, 230 ± 15, and 227 ± 15 km. Note that the lower values of hmF2 correspond to the higher correlation coefficients, due to the larger distance from 325 km.

It is clear from the above that the full range of hmF2 values (i.e., all days within October at all longitudes) needs to be at least 50 km below the CHAMP measurement altitude of ≈325 km in order to fully reflect the strong positive correlation between Δ*Ne* and Δ*hmF*2 as the layer moves up and down in response to PW-modulated tidal influences. Otherwise, there can be positive correlations between Δ*Ne* and Δ*hmF*2 for some ranges of days and longitudes and poor or negative correlations in others, depending on how hmF2 is related to the measurement altitude. This is the case for the other LTs sampled from the TIE-GCM output, namely, 0000, 1600, and 0400 hr; however, we consider the noontime results sufficient to demonstrate that at CHAMP altitudes, vertical oscillation of the F layer is the primary response to PW-modulated tides. The above example also brings out an important point regarding measurement of Δ*Ne* variations; the amplitudes of Δ*Ne* due to PW-modulated tides are significantly diminished if measured near the peak and tend to cancel out in a height-integrated measurement such as total electron content. That is, if the response of the ionosphere due to PW-modulated tides is up and down movement of the F layer without any change in shape, then total electron content measurements do not measure any response at all. Of course, there are other secondary factors that affect how the ionosphere responds (and thus preclude better Δ*Ne*-Δ*hmF*2 correlations), including temperature and composition changes (see paper I) that affect chemical loss rates and plasma diffusion.

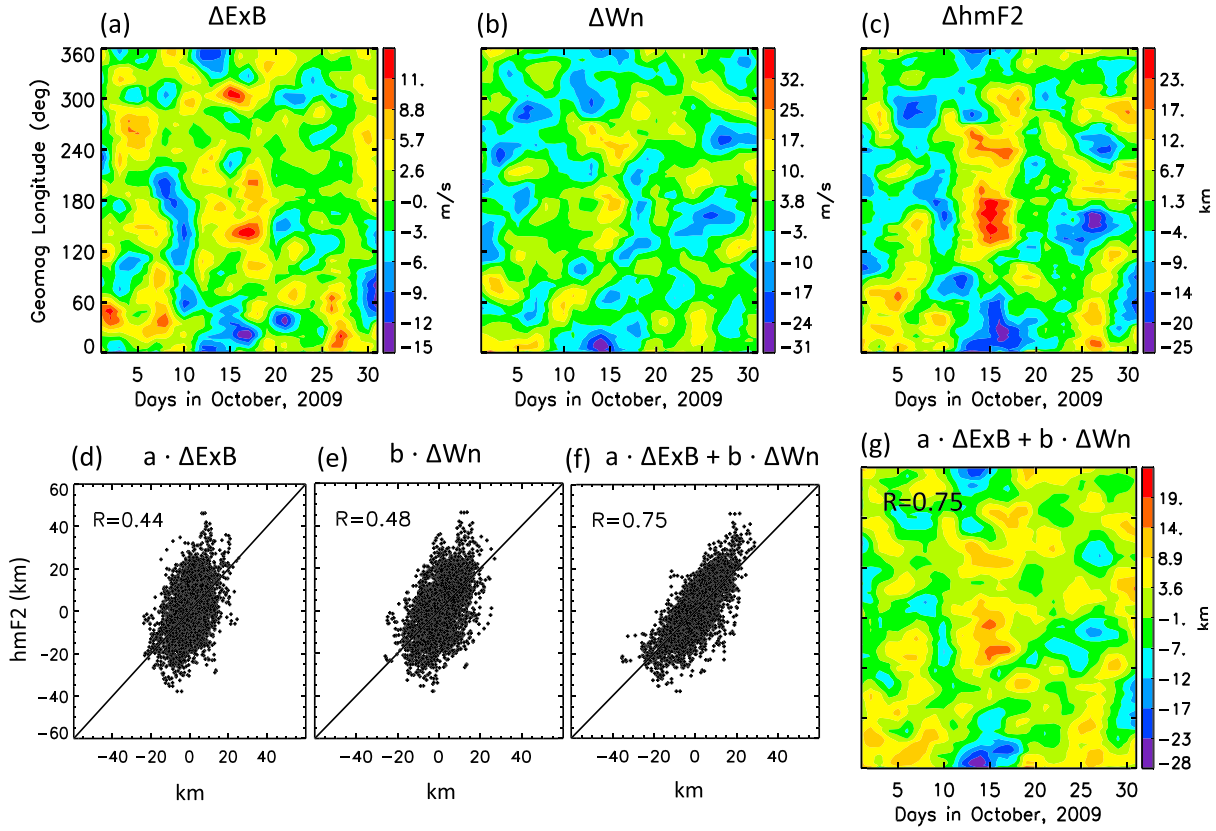


**Figure 4.** Example correlations between ΔhmF2 and ΔE × B vertical plasma drifts and vertical drifts associated with the field-aligned component of neutral winds (ΔWn), in this case for −20° latitude at LT = 1200 hr. (a) ΔE × B; (b) ΔWn; (c) ΔhmF2; (d) scatter plot showing correlation between ΔhmF2 and ΔE × B; (e) scatter plot showing correlation between ΔhmF2 and ΔWn; (f) scatter plot showing correlation between ΔhmF2 and $a \cdot \Delta E \times B + b \cdot \Delta Wn$. (g) shows the reconstruction based on $a \cdot \Delta E \times B + b \cdot \Delta Wn$, which can be compared (c). Similar figures at −40°, −20°, 0°, +20°, and +40° latitude for both LT = 1200 hr and LT = 0000 hr are contained in Figure S4. LT = local time.

Similar correlations of Δ*Ne* with changes in [O]/[$N_2$] ratio and $N_2$ concentrations were investigated (as in Figure 3), and in virtually all cases (for one exception, see below), no attributions to chemical changes could be found whatsoever. The changes in [O] and [$N_2$] due to *tides alone* at 325 km (not shown) generally fell in the range ±3% and ±15%, respectively, and chemical time constants are comparatively large above the F-region peak. Therefore, it should not be surprising that in terms of transmitting the effects of PW-modulated tides on the ionosphere, that dynamical influences outweigh chemical effects at and above the F-region peak. Also, as noted in paper I, while some of the chemical changes are correlated with those in temperature, thus indicating a connection to hydrostatic balance, another contribution arises from changes in the zonal mean circulation driven by the dissipating tides. The latter occurs on a time scale of order 9 days and thus is not an important contributor to chemical changes driven by PW-modulated tides at shorter time scales.

Returning to the noontime analysis, we now seek to determine to what extent hmF2 changes at PW periods are attributable to E × B drifts versus neutral winds. Some typical results are shown in Figure 4, which corresponds to LT = 1200 hr and −20° magnetic latitude. (Similar results at other latitudes for LT = 1200 hr and LT = 0000 hr can be found in Figure S4.) Figure 4a shows the longitude versus day-of-month variations in ΔE × B vertical plasma drifts, and Figure 4b similarly shows the vertical plasma drifts due to the neutral wind; that is, the vertical projection of the field-aligned component of the horizontal neutral wind vector. Figure 4c illustrates the longitude versus day-of-month variability of ΔhmF2, which is identical to Figure 3a. Figures 4d–4f show respectively how ΔhmF2 correlates individually with ΔE × B ($R = +0.44$) and ΔWn ($R = +0.48$) and in combination ($R = +0.75$). Finally, Figure 4g illustrates the longitude versus day-of-month reconstruction of ΔhmF2 based on $a \cdot \Delta E \times B + b \cdot \Delta Wn$, which can be compared with Figure 4c.

Comparing Figures 4g and 4c, it is obvious that many salient features of the ΔhmF2 variability are captured by the reconstruction. However, the $R = +0.75$ correlation means that only $R^2 \times 100 = 56\%$ of the variance in

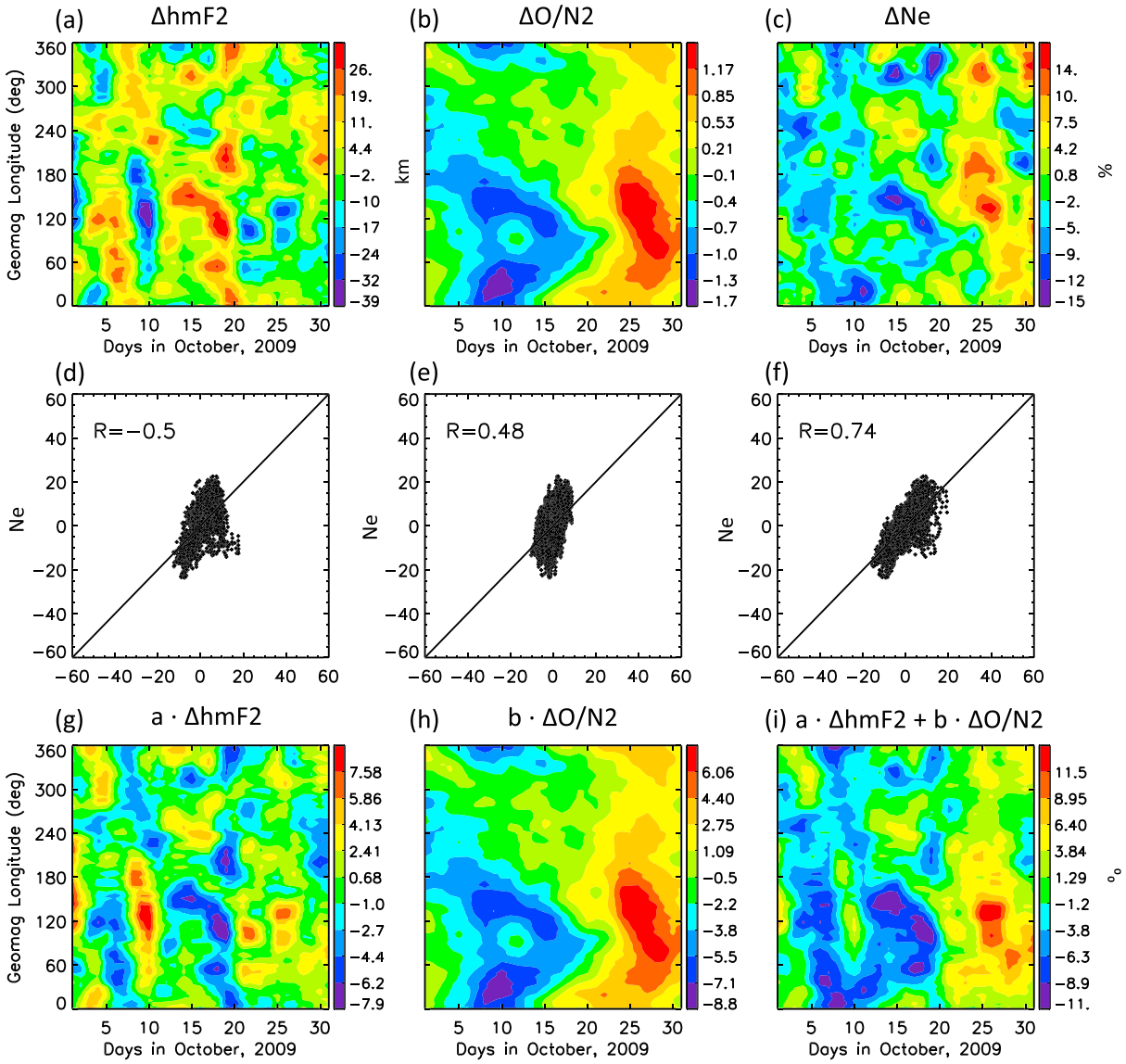


**Figure 5.** Example correlations between ΔNe and ΔhmF2 and $\Delta[O]/[N_2]$, in this case for the magnetic equator at local time = 1600 hr. (a) ΔhmF2; (b) $\Delta[O]/[N_2]$; (c) ΔNe; (d) scatter plot showing correlation between ΔNe and ΔhmF2; (e) scatter plot showing correlation between ΔNe and $\Delta[O]/[N_2]$; (f) scatter plot showing correlation between ΔNe and $a \cdot \Delta hmF2 + b \cdot \Delta[O]/[N_2]$. (g)–(i) show the reconstructions corresponding to (d)–(f), respectively, which can be compared with (c).

ΔhmF2 is captured, with ΔE × B and ΔWn contributing about equally. Perhaps not unexpectedly, we did find (see Figure S4) that E × B drifts were the dominant contributor to ΔhmF2 at the magnetic equator, while Wn was a more equal contributor at ±40° latitudes; moreover, at LT = 0000-hr correlation, coefficients with winds and E × B drifts combined were generally closer to +0.90 (81% of the variance in ΔhmF2 accounted for), and neutral winds were dominant at ±20° and ±40° latitudes. These results for LT = 0000 hr, combined with the servo model and the above results for LT = 1200 hr, provide additional but indirect evidence that substantial topside ΔNe variability at PW periods accompanies hmF2 changes during nighttime. It is conjectured that much of the remaining 44% of the variance in ΔhmF2 during daytime at ±20° latitude may be accounted for by the downward diffusion of plasma associated with formation of the equatorial ionization anomalies, which is also likely modulated by PW variations in equatorial E × B, but not necessarily synchronized with local E × B variations. Also, the time-varying ion drag associated with this diffusion can modify the meridional wind field (Maruyama et al., 2003) and degrade the simple ΔWn-ΔhmF2 relationship inferred from the servo model. There are also secondary influences such as the temperature-dependent diffusion coefficients that are influenced by temperature changes (see paper I) associated with PW-tide modulation.

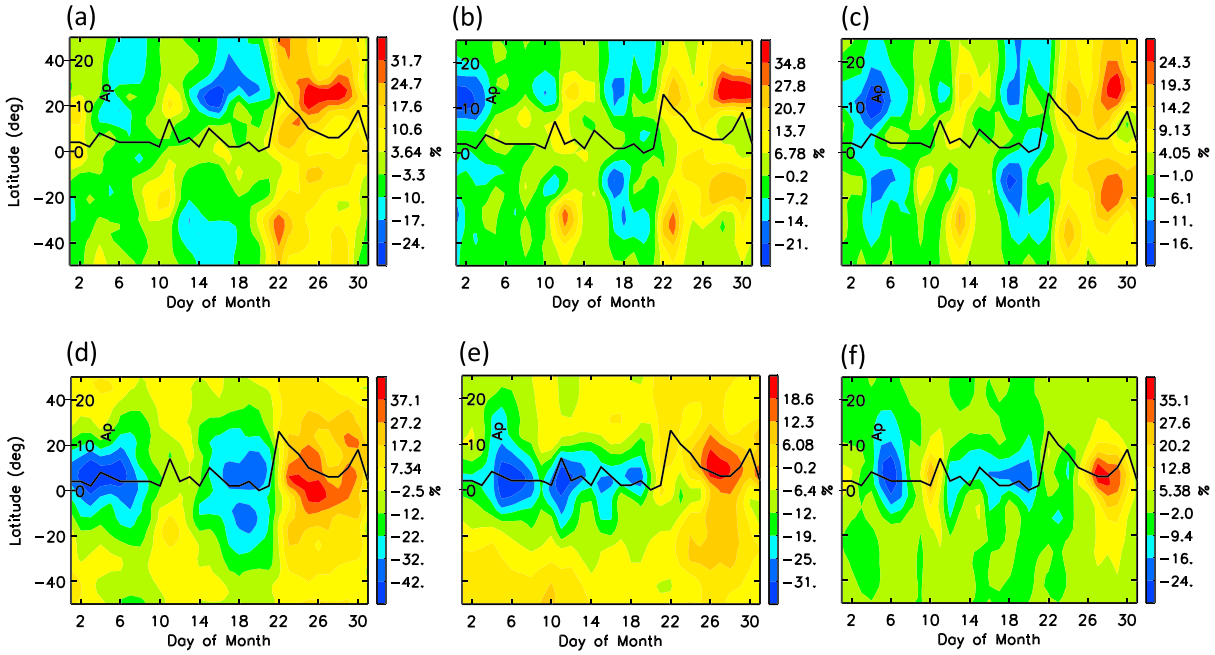


**Figure 6.** Comparisons between S0 oscillations in Ne derived from CHAMP measurements and those from the reference TIE-GCM simulation displayed in a geographic latitude versus day-of-month format. The displayed quantities are zonal means of percent residuals from 27-day running means in order to better highlight the oscillations at planetary-wave periods. (a) CHAMP S0 corresponding to a mean local time ≈ 1600 hr. (b) S0 based on TIE-GCM sampled according to CHAMP sampling. (c) S0 based on fully sampled TIE-GCM output. (d)–(f) are the same as (a)–(c) except for 0400 hr local time. The solid black lines represent the daily Ap magnetic index. Note that different color scales are used in each panel to highlight the S0 oscillations, but differences in absolute magnitude exist. TIE-GCM = thermosphere ionosphere electrodynamics general circulation model.

The important revelation that resides in the above results is the relatively strong influence exerted in situ in the F region by PW-modulated tidal winds, in comparison to the E × B drift effects that originate in the E region through the dynamo generation of electric fields. As outlined in the section 1, it has been commonplace in the literature to ascribe PW oscillations in the F-region ionosphere to the latter mechanism, whether it be due to the direct influence of PW winds or to PW-modulated tidal winds in the E region. While the dynamo mechanism is certainly operative and important, the present results provide an alternative perspective on PW-period variability of the ionosphere and further insight into the complexity of atmosphere-ionosphere coupling.

Additional insights into the complexity of PW-driven atmosphere-ionosphere coupling is provided by Figure 5, which illustrates relationships between hmF2, $[O]/[N_2]$ ratio, and Ne at 325 km for LT = 1600 hr at the magnetic equator. However, the servo model is not applicable at the equator, since the fundamental assumption leading to equation (3) that horizontal gradients in Ne are negligible is violated in the vicinity of the magnetic equator (Rishbeth, 2000). Nevertheless, this example is of interest since it is one of the few that showed any effects related to chemical composition, and it also corresponds to a mean altitude of hmF2 (330 ± 35 km) above 325 km. Therefore, we proceed to see what kinds of relationships exist between ΔNe, ΔhmF2, and $\Delta[O]/[N_2]$.

The top row of Figure 5 illustrates the longitude versus day-of-month variability of ΔhmF2 (Figure 5a), $\Delta[O]/[N_2]$ (Figure 5b), and ΔNe (Figure 5c). In the second row, Figures 5d – 5f show scatter plots and correlation coefficients corresponding to the linear correlation between ΔNe and ΔhmF2, $\Delta[O]/[N_2]$, and $a \cdot \Delta\text{hmF2} + b \cdot \Delta[O]/[N_2]$, respectively. Figures 5g – 5i show the reconstructions of ΔhmF2, $\Delta[O]/[N_2]$, and ΔNe based on the linear relationships derived from the least-squares fits.

In Figure 5, note the negative linear correlation ($R = -0.50$) between ΔNe and ΔhmF2, which is consistent with the fact that 325 km is sufficiently below many of the 27-day mean values of hmF2 during October 2009 and across the full range of longitudes (refer to Figure S3b). Despite the relatively low correlation coefficient, the anticorrelation between ΔNe and ΔhmF2 is visually evident by comparing Figures 5c and 5a. As discussed in connection with Figure 3, the level of anticorrelation is significantly degraded due to the relative proximity of

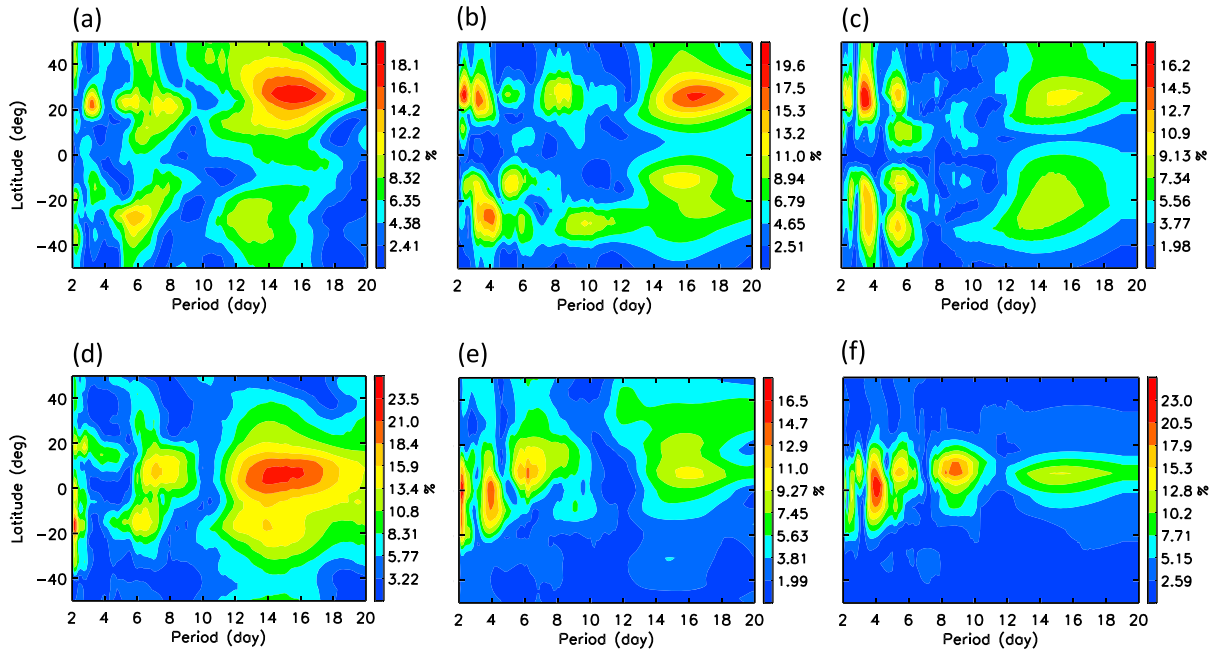


**Figure 7.** Latitude versus wave period spectra of the S0 oscillations depicted in Figure 6. Note that different color scales are used in each panel to highlight the S0 oscillations, but differences in absolute magnitude exist.

325 km to many of the hmF2s during this time frame and span of longitudes. Also, note the positive correlation ($R = +0.48$) between ΔNe and $\Delta[O]/[N_2]$, which likely arises due to the fact that chemical time constants are relatively short below hmF2 and that vertical diffusion is impeded at the magnetic equator. It is also noteworthy that the sum $a \cdot \Delta\text{hmF2} + b \cdot \Delta[O]/[N_2]$ correlates with ΔNe at $R = +0.74$, thus capturing 55% of the variance. It is likely that a significant fraction of the remaining 45% is attributable to the proximity of hmF2s to 325 km as just mentioned.

### 3.3. CHAMP Measurements and Interpretations

The CHAMP satellite carried a Planar Langmuir Probe which measured electron densities at 0.067 Hz, and these data have been utilized in recent studies of the ionosphere (e.g., Xiong & Lühr, 2014; Zhou et al., 2016) and validated against digisonde observations at Jicamarca (McNamara et al., 2007). In light of paper I and the ground-based study by Borries and Hoffmann (2010) that revealed prominent S0 oscillations of the ionosphere at PW periods, the emphasis here is placed on S0 oscillations in the CHAMP data and in our numerical experiments.

Figure 6 compares the S0 oscillations in Ne derived from CHAMP measurements with those from the *reference* TIE-GCM simulation displayed in a latitude versus day-of-month format. Note that different color scales are used in each panel (and in Figure 7 to be described below) to highlight the S0 oscillations, but differences in absolute magnitude exist. The top row (Figures 6a–6c) corresponds to LT = 1600 hr and the bottom row (Figures 6d–6f) to 0400 hr, the mean LTs of the ascending and descending parts of the CHAMP orbit during October 2009. Figures 6a and 6d display the CHAMP data; Figures 6b and 6e display the corresponding S0 oscillations from the TIE-GCM output sampled in UT and longitude according to CHAMP sampling; and Figures 6c and 6f are the S0 oscillations derived from the fully sampled TIE-GCM output. The model and observations share some broad similarities: The 0400-hr oscillations maximize at the equator, while the 1600-hr oscillations tend to maximize on both sides of the equator and somewhere between 20° and 40° latitude; the positive and negative oscillations in Ne are in phase between the model and observations; and the response to the increase in Ap to a value of 12 around 22 October is notable. There are some differences between the fully sampled and CHAMP-sampled model results, which can serve as a measure of the veracity of the CHAMP S0 oscillations, which appear to be affected to some degree by the ~24° longitude sampling imposed by the orbital period of CHAMP. It is also noteworthy that in comparison with the fully sampled model results, the CHAMP sampling tends to amplify the overall intensity of the S0 oscillations at 1600 hr, while the reverse is true at 0400 hr.

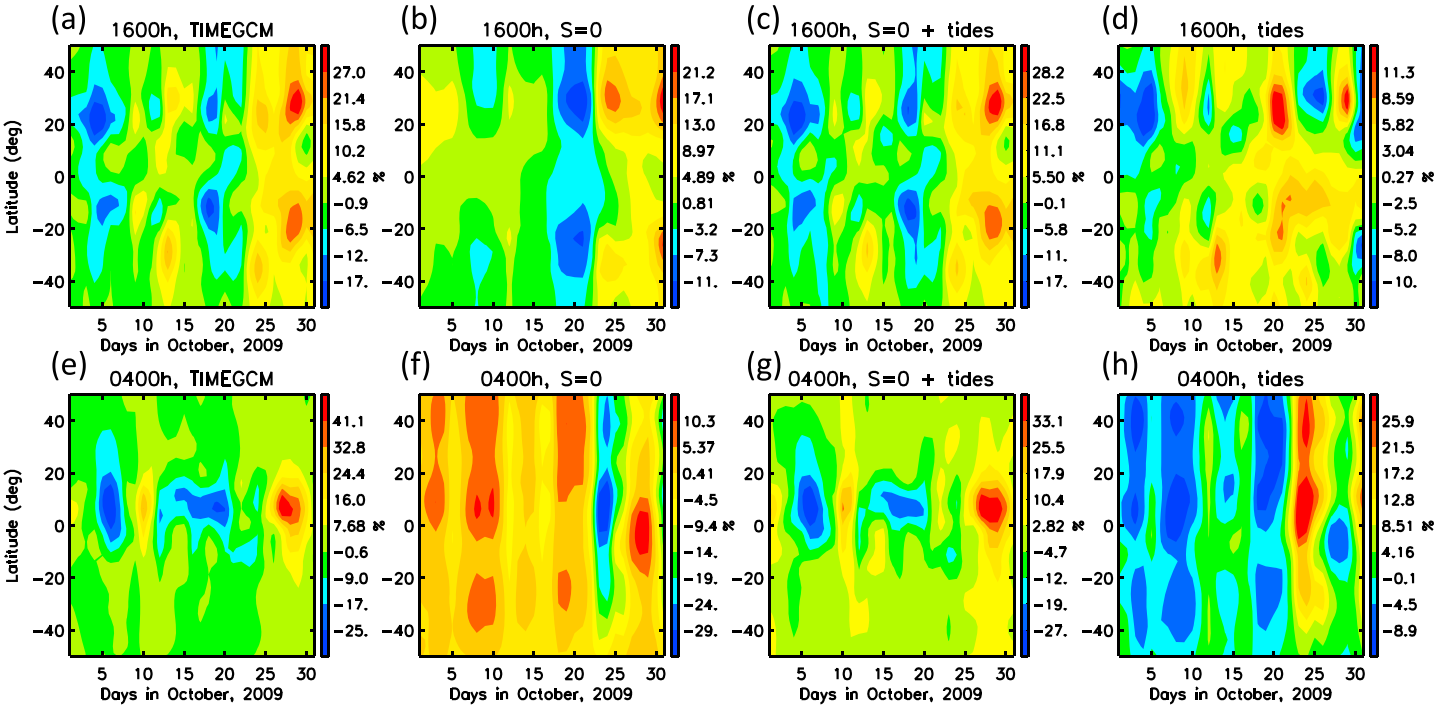


**Figure 8.** Same as Figure 1, except for S0 oscillations plotted versus latitude. TIME-GCM = thermosphere-ionosphere-mesosphere-electrodynamics general circulation model.

Figure 7 provides a complementary view, where the latitude versus wave period spectra of the S0 oscillations in Figure 6 are illustrated. Similar periodicities and amplitudes appear in both the observations and model, and the double-peaked structures in latitude at 1600 hr and tendencies toward the more equatorial and single-peaked confinement of the oscillations at 0400 hr are reflected here as well. In all, it can be said that the TIE-GCM captures most of the salient features that reside in the observations, although some differences in amplitudes exist. Now we seek to establish the contributions and relative importance of PW-modulated tides in producing the S0 oscillations.

As in Figure 1, Figure 8 provides outputs based on the numerical experiments, except here the focus is on the S0 oscillations. In this case, the $s = 0$ forcing results in Figures 8b and 8f are particularly relevant, since they primarily reflect the part of the total response (indicated in Figures 8a and 8e; replicated from Figures 6c and 6f) driven in situ by variable but low-level magnetic activity. The max to min range (or peak-to-peak variability) of this response between ±50° latitude during the whole month of October is about 32% at 1600 hr and 39% at 0400 hr and is mainly confined to the period between days 20–30 when the largest changes in Ap occur. The corresponding ranges for the total response from the reference simulation (Figures 8a and 8e) are 44% and 66%, respectively, indicating that there is another source of S0 variability that must be accounted for. Comparing the response to $s = 0$ forcing + tides (Figures 8c and 8g) with the reference simulation, the excellent agreement between the two indicates that this additional source is provided by the presences of tides; specifically, the dissipation of tides that are modulated at PW periods, as demonstrated in paper I and reviewed in the section 1 to the present paper. Figures 8d and 8h quantify these tidal contributions, which reveal response ranges as defined above of order 21% at 1600 hr and 35% at 0400 hr, which are similar in magnitude to the 32% and 39% ranges attributable to $s = 0$ forcing alone. Note also that the higher relative magnitudes at night versus day reflect the smaller 27-day mean reference values at night versus day.

Figure 9 examines the nature of the ΔhmF2, ΔWn, and ΔE × B S0 variations at PW periods due exclusively to PW-modulated tides at 0400 hr. Our previous discussions in connection with Figures 3 and 5 inform us that atmosphere-ionosphere coupling due to PW-modulated tides is mainly conveyed by changes in hmF2 and not chemistry, at least at nonequatorial latitudes above hmF2. Very low correlations with $[O]/[N_2]$ and $[N_2]$ were also borne out with respect to the S0 oscillations in Ne. Figure 9 is modeled after Figure 4, except now that variations are plotted in a geographic latitude versus day-of-month frame, instead of a longitude versus day-of-month frame at a constant magnetic latitude. The peak-to-peak variability or range of ΔhmF2

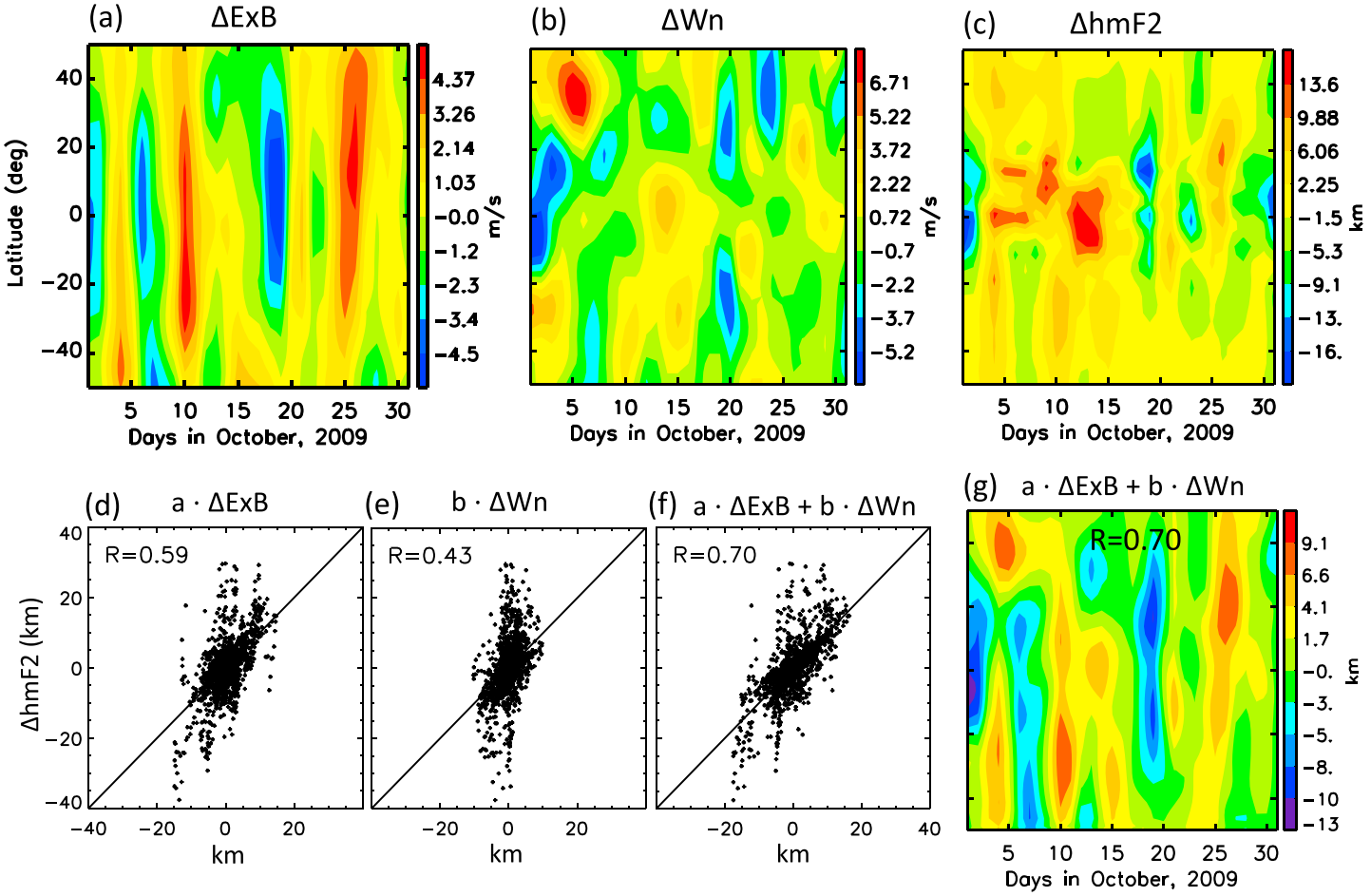


**Figure 9.** Same as Figure 4, except in geographic coordinates for S0 oscillations at 0400 hr.

(Figure 9c) is about 30 km (20 km at 1600 hr, not shown), which can be compared with values associated with all zonal wavenumbers at latitudes −40°, −20°, 0°, +20°, and +40° that range between 30 and 70 km at LT = 1200 hr, 50 and 70 km at LT = 0000 hr, 40 and 80 km at LT = 1600 and 0400 hr. Thus, in crude terms, the S0 variability amounts to roughly half that contributed by all zonal wavenumbers.

Figures 9a and 9b illustrate the S0 oscillations in ΔE × B and ΔWn; some features of both can be seen in Figure 9c which displays ΔhmF2. The correlations between ΔhmF2 and ΔE × B ($R$ = +0.59, Figure 9d) and ΔWn ($R$ = +0.43, Figure 9e) are rather modest, although the combination of the two correlates at $R$ = +0.70 and thus accounts for about 50% of the variability. The reconstruction based on this combined fit in Figure 9g actually captures many salient features depicted in Figure 9c. It is uncertain what level of correlation between ΔhmF2, ΔE × B, and ΔWn one should expect for the S0 oscillations, as opposed to the local situation at a fixed latitude and longitude; for instance, whether the zonal averaging invalidates the linear relationships in the servo model. However, the correlations displayed here are not very different from those displayed in Figure 4, which suggests that the conjectured reasons behind the modest levels of correlation pertain to Figure 4 also apply here. What is interesting here is the existence and relatively important role played by S0 oscillations in E × B, something not previously mentioned in the literature. This finding is discussed further in the next section.

## 4. Concluding Remarks

As in paper I, the present paper employs TIME-GCM/MERRA2009 output for October 2009 to force TIE-GCM at its 97-km lower boundary in a way that enables isolation of the influences of the PW-modulated tidal spectrum on the ionosphere-thermosphere system. This period of time is chosen since it is characterized by a familiar set of nontidal waves, that is, the Q6DW, Q10DW, Q16DW, and an UFKW with period near 3.5 days and $s = -1$.

Paper I focused on the neutral thermosphere response, while the present paper directs its attention to the response of the ionosphere at 325 km. This altitude is chosen in part to maintain consistency with paper I, and also, since it corresponds to the mean altitude of the CHAMP satellite during October 2009. Electron density measurements during October 2009 from the Planar Langmuir Probe instrument on CHAMP are also analyzed and interpreted in the context of the TIE-GCM simulations. Our results and conclusions are summarized as follows:

1. Longitude versus day-of-month variations at PW periods (2 to 20 days) of order ±30–50% in F-region electron density (Ne, at 325 km) at a particular LT occur as a result of PW-modulated tides.
2. When the F-layer peak height (hmF2) is sufficiently below 325 km, it is clear that the above oscillations are mainly due to vertical oscillations in the F layer of order ±15–40 km. Chemical effects generally play a minor role except at or below hmF2. The predominant origins of these vertical movements are E × B drifts and the vertical projection of field-aligned in situ neutral winds. E × B drifts dominate close to the magnetic equator, while the two sources play more equal roles between 20° and 40° magnetic latitudes in each hemisphere. The in situ neutral wind effect arises from vertical propagation of PW-modulated tides, whereas the E × B drifts originate from dynamo-generated electric fields produced by the E-region component of the same wind field; the former represents a previously unappreciated coupling mechanism for production of ionospheric oscillations at PW periods.
3. Roughly half of the Ne variability at PW periods is associated with zonally symmetric (S0) oscillations. This is fundamentally in agreement with the ground-based total electron content analyses of Borries and Hoffmann (2010), except their study was confined to latitudes poleward of 50°N. Borrowing from the terminology of paper I, we can say that the ionosphere *vacillates* in response to the PW-modulated tidal spectrum.
4. In addition to S0 oscillations in hmF2 at PW periods being driven by S0 F-region wind perturbations resulting from dissipation of tides, we also find that S0 E × B drifts are playing an equally important role in accounting for hmF2 variability. Generally, dynamo-region S0 winds are not thought to produce electric fields since they do not contribute to the divergence of zonal currents (Gan et al., 2016, 2017), which can arise due to zonal asymmetries in winds and/or conductivities (Liu et al., 2010). The existence of S0 oscillations in E × B drifts could thus suggest that zonal asymmetries in conductivity are playing a role. Gan et al. (2017) also demonstrate that Q6DW-modulated tides can produce S0 oscillations in Ne at the F2-layer peak through the chemical effects that they produce. We could not conclusively identify this link in the present simulations. An alternative and perhaps more straightforward explanation is that an S0 component of E × B drift variability at PW periods simply results from modulation of $s = 1$ PW oscillations in E by the wave-1 zonal variation in the magnitude of B. This is analogous to the in situ generation of D0 (along with DW2) at F-region heights due to interaction between DW1 winds and the wave-1 variation of ion drag imposed by the magnetic field (Jones et al., 2013). In the present case the wave periods, of course, belong to the PW instead of the diurnal tide.
5. The TIE-GCM simulates the latitude versus day-of-month S0 oscillations in Ne observed from the CHAMP satellite well during October 2009. We use this result, and the numerical experiments discussed above, to demonstrate that the space-time variability in Ne induced by the PW modulation of tides (peak-to-peak 20% at 1600 hr and 35% at 0400 hr) occurs at a little more than half the magnitude as low-level magnetic activity during October 2009 (peak-to-peak 45% at 1600 hr and 60% at 0400 hr).

**Acknowledgments**
This work was supported by NASA Grant NNX16AG64G to the University of Colorado and through subawards 1554135 and 1554133 to Utah State University and High Altitude Observatory, National Center for Atmospheric Research, respectively. TIME-GCM and TIE-GCM results are archived on the National Center for Atmospheric Research High Performance Storage System and are available on request. We would like to acknowledge high-performance computing support from Cheyenne (https://doi.org/10.5065/D6RX99HX) provided by NCAR's Computational and Information Systems Laboratory, sponsored by the National Science Foundation. The National Center for Atmospheric Research is funded by the National Science Foundation.

## References

Altadill, D. (2000). Planetary wave type oscillations in the ionospheric F region. *Advances in Space Research*, *26*(8), 1287–1296.

Altadill, D., Apostolov, E. M., & Alberca, L. (1997). Some seasonal hemispheric similarities in $f_oF2$ quasi-2-day oscillations. *Journal of Geophysical Research*, *102*(A5), 9737–9739.

Altadill, D., Apostolov, E. M., Jacobi, C., & Mitchell, N. J. (2003). Six-day westward propagating wave in the maximum electron density of the ionosphere. *Annales Geophysicae*, *21*, 1577–1588.

Altadill, D., Apostolov, E. M., Solé, J. G., & Jacobi, C. (2001). Origin and development of vertical propagating oscillations with periods of planetary waves in the ionospheric F region. *Physics and Chemistry of the Earth*, *26*(6), 387–393.

Altadill, D., & Lastovicka, J. (1996). Quasi-five- and ten-day oscillations in $f_oF2$ and their possible connection with oscillations at lower ionospheric heights. *Annales Geophysicae*, *39*(4), 705–712. https://doi.org/10.4401/ag-4001

Apostolov, E. M., Alberca, L., & Altadill, D. (1994). Solar cycle and seasonal behaviour of quasi-two- and five-day oscillations in the time variations of $f_oF2$. *Annales Geophysicae*, *37*, 187–192.

Apostolov, E. M., Altadill, D., & Alberca, L. (1995). Characteristics of quasi-2-day oscillation in $f_oF2$ at northern middle latitudes. *Journal of Geophysical Research*, *100*(A7), 12,162–12,171.

Borries, C., & Hoffmann, P. (2010). Characteristics of $F2$-layer planetary wave-type oscillations in northern middle and high latitudes during 2002 to 2008. *Journal of Geophysical Research*, *115*, A00G10. https://doi.org/10.1029/2010JA015456

Borries, C., Jakowski, N., Jacobi, C., Hoffmann, P., & Pogoreltsev, A. (2007). Spectral analysis of planetary waves seen in ionospheric total electron content (TEC): First results using GPS differential TEC and stratospheric reanalyses. *Journal of Atmospheric and Solar-Terrestrial Physics*, *69*(17-18), 2442–2451. https://doi.org/10.1016/j.jastp.2007.02.004

Buonsanto, M. J., Starks, M. J., Titheridge, J. E., Richards, P. G., & Miller, K. L. (1997). Comparison of techniques for derivation of neutral meridional winds from ionospheric data. *Journal of Geophysical Research*, *102*(A7), 14,477–14,484. https://doi.org/10.1029/97JA01149

Chang, L. C., Yue, J., Wang, W., Wu, Q., & Meier, R. R. (2014). Quasi two day wave-related variability in the background dynamics and composition of the mesosphere/thermosphere, and the ionosphere. *Journal of Geophysical Research: Space Physics*, *119*, 4786–4804. https://doi.org/10.1002/2014JA019936

Chen, P.-R. (1992). Two-day oscillation of the equatorial ionization anomaly. *Journal of Geophysical Research*, *97*(A5), 6343–6357.

Forbes, J. M. (1995). Tidal and planetary waves (A tutorial). In R. M. Johnson & T. L. Killeen (Eds.), *The Upper Mesosphere and Lower Thermosphere: A Review of Experiment and Theory*, *Geophysical Monograph Series* (Vol. 87, p. 356). Washington, DC: American Geophysical Union.

Forbes, J. M. (1996). Planetary waves in the thermosphere-ionosphere system. *Journal of Geomagnetism and Geoelectricity*, *48*, 91–98.

Forbes, J. M., Guffee, R., Zang, X., Fritts, D., Riggin, D., Manson, A., et al. (1997). Quasi 2-day oscillation of the ionosphere during summer 1992. *Journal of Geophysical Research*, *102*(A4), 7301–7305.

Forbes, J. M., Hagan, M. E., Vial, F., Miyahara, S., Manson, A. H., & Portnyagin, Y. U. I. (1995). Quasi-16-day oscillation in the mesosphere and lower thermosphere. *Journal of Geophysical Research*, *100*(D5), 9149–9164.

Forbes, J. M., & Leveroni, S. (1992). Quasi 16-day oscillation in the ionosphere. *Geophysical Research Letters*, *19*(10), 981–984.

Forbes, J. M., Palo, S. E., & Zhang, X. (2000). Variability of the ionosphere. *Journal of Atmospheric and Solar-Terrestrial Physics*, *62*, 685–693.

Forbes, J. M., & Zhang, X. (1997). The quasi 2-day ionospheric oscillation: A statistical study. *Journal of Atmospheric and Solar-Terrestrial Physics*, *59*, 1025–1034.

Forbes, J., Zhang, X., Maute, A., & Hagan, M. E. (2018). Zonally symmetric oscillations of the thermosphere at planetary wave periods. *Journal of Geophysical Research: Space Physics*, *123*, 4110–4128. https://doi.org/10.1002/2018JA025258

Gan, Q., Oberheide, J., Yue, J., & Wang, W. (2017). Short-term variability in the ionosphere due to the nonlinear interaction between the 6 day wave and migrating tides. *Journal of Geophysical Research: Space Physics*, *122*, 8831–8846. https://doi.org/10.1002/2017JA023947

Gan, Q., Wang, W., Yue, J., Liu, H., Chang, L. C., Zhang, S., et al. (2016). Numerical simulation of the 6-day wave effects on the ionosphere: Dynamo modulation. *Journal of Geophysical Research: Space Physics*, *121*, 10,103–10,116. https://doi.org/10.1002/2016JA022907

Gan, Q., Yue, J., Chang, L. C., Wang, W. B., Zhang, S. D., & Du, J. (2015). Observations of thermosphere and ionosphere changes due to the dissipative 6.5-day wave in the lower thermosphere. *Annales Geophysicae*, *33*(7), 913–922. https://doi.org/10.5194/angeo-33-913-2015

Gu, S.-Y., Liu, H., Dou, X., & Jia, M. (2018). Ionospheric variability due to tides and quasi-two day wave interactions. *Journal of Geophysical Research: Space Physics*, *123*, 1554–1565. https://doi.org/10.1002/2017JA025105

Gurubaran, S., & Sridharan, R. (1993). Effect of meridional winds and neutral temperatures on the *F* layer heights over low latitudes. *Journal of Geophysical Research*, *98*(A7), 11,629–11,635. https://doi.org/10.1029/92JA02029

Hagan, M. E., Forbes, J. M., & Vial, F. (1993). Numerical investigation of the propagation of the quasi-two-day wave into the lower thermosphere. *Journal of Geophysical Research*, *98*(D12), 23,193–23,205.

Häusler, K., Hagan, M. E., Baumgaertner, A. J. G., Maute, A., Lu, G., Doornbos, E., et al. (2014). Improved short-term variability in the thermosphere-ionosphere-mesosphere-electrodynamics general circulation model. *Journal of Geophysical Research: Space Physics*, *119*, 6623–6630. https://doi.org/10.1002/2014JA020006

Häusler, K., Hagan, M. E., Forbes, J. M., Zhang, X., Doornbos, E., Bruinsma, S., & Lu, G. (2015). Intraannual variability of tides in the thermosphere from model simulations and in situ satellite observations. *Journal of Geophysical Research: Space Physics*, *120*, 751–765. https://doi.org/10.1002/2014JA020579

Huang, Y.-N., Cheng, K., & Chen, S.-W. (1989). On the equatorial anomaly of the ionospheric total electron content near the northern anomaly crest region. *Journal of Geophysical Research*, *94*(A10), 13515–13525. https://doi.org/10.1029/JA094iA10p13515

Ito, R., Kato, S., & Tsuda, T. (1986). Consideration of an ionospheric wind dynamo driven by a planetary wave with a two-day period. *Journal of Atmospheric and Solar-Terrestrial Physics*, *48*(1), 1–13.

Jones, Jr. M., Forbes, J. M., Hagan, M. E., & Maute, A. (2013). Non-migrating tides in the ionosphere-thermosphere: In situ versus tropospheric sources. *Journal of Geophysical Research: Space Physics*, *118*, 2438–2451. https://doi.org/10.1002/jgra.50257

Laštovička, J., & Šauli, P. (1999). Are planetary wave type oscillations in the F2 region caused by planetary wave modulation of upward propagating tides? *Advances in Space Research*, *24*(11), 1473–1476.

Laštovička, J., Šauli, P., & Križan, P. (2006). Persistence of planetary wave type oscillations in the mid-latitude ionosphere. *Annales Geophysicae*, *49*(6), 1235–1246.

Laundal, K. M., & Richmond, A. D. (2016). Magnetic coordinate systems. *Space Science Reviews*, *206*(1–4), 27–59. https://doi.org/10.1007/s11214-016-0275-y

Lei, J., Thayer, J., Forbes, J. M., Wu, Q., She, C., Wan, W., & Wang, W. (2008). Ionosphere response to solar wind high-speed streams. *Geophysical Research Letters*, *35*, L19105. https://doi.org/10.1029/2008GL035208

Liu, H.-L., Wang, W., Richmond, A. D., & Roble, R. G. (2010). Ionospheric variability due to planetary waves and tides for solar minimum conditions. *Journal of Geophysical Research*, *115*, A00G01. https://doi.org/10.1029/2009JA015188

Liu, H.-L., Yudin, V. A., & Roble, R. G. (2013). Day-to-day ionospheric variability due to lower atmosphere perturbations. *Geophysical Research Letters*, *40*, 665–670. https://doi.org/10.1002/grl.50125

Maruyama, N., Watanabe, S., & Fuller-Rowell, T. J. (2003). Dynamic and energetic coupling in the equatorial ionosphere and thermosphere. *Journal of Geophysical Research*, *108*(A11), 1396. https://doi.org/10.1029/2002JA009599

McLandress, C., & Mcfarlane, N. A. (1993). Interactions between orographic gravity wave drag at forced stationary planetary waves in the winter northern hemisphere middle atmosphere. *Journal of the Atmospheric Sciences*, *50*, 1966–1990.

McNamara, L., Cooke, D. L., Valladares, C. E., & Reinisch, B. W. (2007). Comparison of CHAMP and digisonde plasma frequencies at Jicamarca, Peru. *Radio Science*, *42*, RS2005. https://doi.org/10.1029/2006RS003491

Mendillo, M., Rishbeth, H., Roble, R. G., & Wroten, J. (2002). Modelling F2-layer seasonal trends and day-to-day variability driven by coupling with the lower atmosphere. *Journal of Atmospheric and Solar-Terrestrial Physics*, *64*, 1911–1931.

Meyer, C. K. (1999). Gravity wave interactions with mesospheric planetary waves: A mechanism for penetration into the thermosphere-ionosphere system. *Journal of Geophysical Research*, *104*(A12), 28,181–28,196. https://doi.org/10.1029/1999JA900346

Miller, K. L., Torr, D. G., & Richards, P. G. (1986). Meridional winds in the thermosphere derived from measurement of $F_2$ layer height. *Journal of Geophysical Research*, *91*(A4), 4531–4535.

Miyahara, S. (1985). Suppression of stationary planetary waves by internal gravity waves in the mesosphere. *Journal of the Atmospheric Sciences*, *42*, 100–107.

Nguyen, V., & Palo, S. E. (2014). Transmission of planetary wave effects to the upper atmosphere through eddy diffusion modulation. *Journal of Atmospheric and Solar-Terrestrial Physics*, *117*, 1–6.

Nystrom, V., Gasperini, F., Forbes, J. M., & Hagan, M. E. (2018). Exploring wave-wave interactions in a general circulation model. *Journal of Geophysical Research: Space Physics*, *123*, 827–847. https://doi.org/10.1002/2017JA024984

Pancheva, D. (1988). Traveling quasi-two-day fluctuations in the summer F-region. *Comptes Rendus de l'Académie Bulgare des Sciences*, *41*, 41–44.

Pancheva, D., Alberta, L. F., & de la Morena, B. A. (1994). Simultaneous observation of the quasi-two day variations in the lower and upper ionosphere. *Journal of Atmospheric and Terrestrial Physics*, *56*, 43–50.

Pancheva, D., & Lysenko, I. (1988). Quasi two-day fluctuations observed in the summer *F* region electron maximum. *Bulgarian Geophysical Journal*, *14*, 41–51.

Parish, H. F., Forbes, J. M., & Kamalabadi, F. (1994). Planetary wave and solar emission signatures in the equatorial electrojet. *Journal of Geophysical Research*, *99*(A1), 355–368.

Richmond, A. D. (1995). Ionospheric electrodynamics using magnetic apex coordinates. *Journal of Geomagnetism and Geoelectricity*, *47*, 191–212.

Rishbeth, H. (1967). The effect of winds on the ionospheric *F*2 peak. *Journal of Atmospheric and Terrestrial Physics*, *29*, 225–238.

Rishbeth, H. (1968). The effect of winds on the ionospheric *F*2 peak–II. *Journal of Atmospheric and Terrestrial Physics*, *30*, 63–71.

Rishbeth, H. (2000). The equatorial F-layer: Progress and puzzles. *Annales Geophysicae*, *18*(7), 730–739.

Rishbeth, H. (2006). F-region links with the lower atmosphere? *Journal of Atmospheric and Solar-Terrestrial Physics*, *68*, 469–478.

Rishbeth, H., Ganguly, S., & Walker, J. C. G. (1978). Field-aligned and field-perpendicular velocities in the ionospheric *F*2-layer. *Journal of Atmospheric and Terrestrial Physics*, *40*, 767–784.

Rishbeth, H., & Mendillo, M. (2001). Patterns of ionospheric variability. *Journal of Atmospheric and Solar-Terrestrial Physics*, *63*, 1661–1680.

Rishbeth, H., Mendillo, M., Wroten, J., & Roble, R. G. (2009). Day-by-day modelling of the ionospheric F2-layer for year 2002. *Journal of Atmospheric and Solar-Terrestrial Physics*, *71*, 848–856.

Salby, M. L. (1981). Rossby normal modes in nonuniform background configurations. Part II: Equinox and solstice conditions. *Journal of the Atmospheric Sciences*, *38*, 1827–1840.

Xiong, C., & Lühr, H. (2014). The mid-latitude summer night anomaly as observed by CHAMP and GRACE: Interpreted as tidal features. *Journal of Geophysical Research: Space Physics*, *119*, 4905–4915. https://doi.org/10.1002/2014JA019959

Yue, J., & Wang, W. B. (2014). Changes of thermospheric composition and ionospheric density caused by quasi 2 day wave dissipation. *Journal of Geophysical Research: Space Physics*, *119*, 2069–2078. https://doi.org/10.1002/2013JA019725

Yue, J., Wang, W., Richmond, A. D., & Liu, H.-L. (2012). Quasi-two-day wave coupling of the mesosphere and lower thermosphere-ionosphere in the TIME-GCM: Two-day oscillations in the ionosphere. *Journal of Geophysical Research*, *117*, A07305. https://doi.org/10.1029/2012JA017815

Yue, J., Wang, W., Richmond, A. D., Liu, H.-L., & Chang, L. C. (2013). Wavenumber broadening of the quasi 2 day planetary wave in the ionosphere. *Journal of Geophysical Research: Space Physics*, *118*, 3515–3526. https://doi.org/10.1002/jgra.50307

Yue, J., Wang, W., Ruan, H., Chang, L., & Lei, J. (2016). Impact of the interaction between the quasi-2 day wave and tides on the ionosphere and thermosphere. *Journal of Geophysical Research: Space Physics*, *121*, 3555–3563. https://doi.org/10.1002/2016JA022444

Zhou, Y.-L., Wang, L., Xiong, C., Lühr, H., & Ma, S.-Y. (2016). The solar activity dependence of non-migrating tides in electron density at low and middle latitudes observed by CHAMP and GRACE. *Annales Geophysicae*, *34*, 463–472. https://doi.org/10.5194/angeo-34-463-2016